

Exciton Linewidth and Exciton-Phonon Coupling in 2H and 3R Bilayer WS₂ Studied by Magnetic Circular Dichroism Spectrum

Nai Jiang, Jia Shi, Heng Wu, Dong Zhang, Hui Zhu, Xinfeng Liu, Ping-Heng Tan, Kai Chang, Houzhi Zheng, and Chao Shen*

Layered transition metal dichalcogenides (TMDs) are a promising platform for new photonic and optoelectronic devices. Exciton-phonon interaction is critical in determining their characteristics such as the exciton coherence lifetime and linewidth. However, the exciton linewidth obtained by conventional reflection spectrum is greatly affected by the background signals, and the research into exciton-phonon coupling difference induced by stacking-order in multi-layer structures is still lacking. In this work, the temperature-dependent exciton linewidths of CVD-grown large-area monolayer, 2H and 3R-stacking bilayer WS₂ based on a self-designed reflective magnetic circular dichroism (MCD) spectrum are systematically investigated. It is found that 2H-bilayer WS₂ exhibits significantly larger exciton linewidth compared with monolayer and 3R bilayer, which can be attributed to the appearance of new phonon-assisted relaxation channels caused by interlayer coupling. Meanwhile, 3R bilayer with a redshifted exciton peak has a narrower linewidth than 2H phase because the interlayer hopping is suppressed, resulting in the absence of interlayer scattering channel. These results provide intuitive evidence for the exciton linewidth-broadening and exciton-phonon coupling in different stacked layers and open up new vistas for the development of TMD-based narrow-linewidth nano-sensors devices.

nanoelectronics and optoelectronics application.^[1–3] When thinned down to monolayer, the band structure of 2D TMDs changes from indirect bandgap to direct.^[4,5] As a result of quantum confinement effect and reduced dielectric screening, the exciton that consisting of tightly bound electron and hole can stably exist even at room temperature with the binding energy of hundreds of meV.^[6–11] It is worth noting that exciton-phonon coupling dominates many optical responses of monolayer TMDs due to significant excitonic effect. For instance, it leads to the decay of non-radiative excitons,^[12,13] mediates the spin flipping processes thus reducing the lifetime of spin/valley-polarized charge carriers,^[14] and is responsible for the decrease of fluorescence quantum yield.^[15] In addition, exciton-phonon coupling controls many aspects of optoelectronic properties in 2D TMDs, such as temperature-dependent bandgap renormalization,^[16] carrier transport,^[17,18] and intervalley scattering of electrons and excitons.^[19,20] It has been demonstrated that the existence of

1. Introduction

Atomically thin layered transition-metal dichalcogenides (TMDs) have become the hotspot of research over the past few years due to their unique optical and transport characteristics in

intervalley dark excitons leads to possible intervalley scattering via phonon assistance, which has a significant impact on the issue of linewidth broadening in 2D TMDs, particularly in tungsten-based WS₂, whose intervalley dark excitonic state is located energetically below the bright excitonic state.^[21–23]

N. Jiang, H. Wu, D. Zhang, H. Zhu, P.-H. Tan, K. Chang, H. Zheng, C. Shen

State Key Laboratory for Superlattices and Microstructures
Institute of Semiconductors
Chinese Academy of Sciences
Beijing 100083, China
E-mail: shenchao@semi.ac.cn

N. Jiang, H. Wu, D. Zhang, P.-H. Tan, K. Chang, H. Zheng, C. Shen
Center of Materials Science and Optoelectronics Engineering
University of Chinese Academy of Sciences
Beijing 100049, China

J. Shi
Institute of Information Photonics Technology and School of Physics and Optoelectronics
Faculty of Science
Beijing University of Technology
Beijing 100124, China

X. Liu
CAS Key Laboratory of Standardization and Measurement for Nanotechnology
CAS Center for Excellence in Nanoscience
National Center for Nanoscience and Technology
Beijing 100190, China

 The ORCID identification number(s) for the author(s) of this article can be found under <https://doi.org/10.1002/adom.202300458>

DOI: 10.1002/adom.202300458

However, there is limited understanding of the detailed exciton-phonon scattering mechanism underlying the linewidth broadening of few-layer WS_2 systems. Since exciton peaks are usually superimposed on some background signals in reflection spectroscopy measurements, which show a relatively complex spectrum, there is uncertainty in the linewidth obtained under the condition of directly fitting the spectrum. Therefore, accurate temperature-dependent linewidth analysis dominated by exciton-phonon coupling is in great demand for future optoelectronic application in many-particle system.

Meanwhile, recent advances in growth and stacking techniques have also switched the attention to few-layer systems.^[24–28] When assembling TMDs monolayers to form multilayers, a lot of novel physical properties can be accessed due to the variation of electronic band structures and symmetry.^[29] Semiconducting multilayer MX_2 (M represents Mo or W and X represents S or Se) can be divided into 2H and 3R phase based on their stacking orders. It is worth mentioning that some intriguing phenomena have been reported in different stacked bilayer MX_2 . Paradisanos et al. verified that only 2H stacking MoS_2 allows for hole delocalization over the bilayer, which results in strong interlayer exciton absorption and a larger A-B exciton separation compared to 3R bilayers.^[30] Schneider et al. demonstrated that 3R-stacked WS_2 bilayer displays larger valley polarization with the spin-valley locking optical transition selection rules rather than the spin-layer locking in 2H-stacked WS_2 .^[31] And Shinde et al. convincingly revealed that the different stacking-order induces the variation of electronic band structure.^[29] Besides, the exciton linewidth as a vital parameter in exploring light-matter interactions in 2D TMDs can be affected by the specific substrate,^[32] strain,^[33] and nanosphere-supported Mie resonances,^[34] but there have been few studies to investigate the connection between the stacking order and exciton linewidth. Therefore, it is necessary to identify the physical mechanisms that how the stacking order in bilayer systems influence the linewidth-broadening, which will open up the possibility to design narrower-linewidth multilayer optoelectronic devices.

In this work, we investigated the temperature-dependent exciton linewidths of CVD-grown large-area monolayer, 2H and 3R phase bilayer WS_2 by self-designed reflective magnetic circular dichroism (MCD) spectrum. By analyzing the quantitative results of exciton-phonon coupling strength that extracted from the temperature-dependent MCD spectra, we revealed that the bilayer WS_2 exhibits larger linewidth broadening than monolayer because of the appearance of new phonon-assisted relaxation channels originated from the interlayer coupling in bilayer. What's more, we discovered that 3R-stacking bilayer WS_2 with a redshift A-exciton peak position displays narrower linewidth in contrast to 2H-stacking, this is because different stacking-order leads to the difference of interlayer-coupling and 2H-stacking bilayer has an extra interlayer scattering pathway within K-valley. Our work provides a new avenue for developing future optoelectronic devices based on 3R stack-oriented multilayer systems, which provide narrower emission linewidths.

2. Results and Discussion

Here, we studied the linewidth broadening of CVD-grown monolayer and two-type bilayer WS_2 with self-built MCD system.^[35]

Generally, 2H phase multi-layer TMDs is the most common and relatively stable phase. Both artificial folding of monolayers or mechanical exfoliation of bulk materials to obtain 3R phase bilayers have disadvantages such as uncontrollable layer, complex process, and small area.^[36–38] Herein, we obtained a large area of stable 3R and 2H-stacking bilayer WS_2 grown on Si substrates with a 150 nm oxide layer via chemical vapor deposition (CVD) growth method. **Figure 1a** and **Figure S1a** (Supporting Information) exhibit the atomic structure (side view) and optical image of 2H and 3R-stacking bilayer WS_2 . The 2H phase is in an AB stacking order with the recovered inversion symmetry, and the A layer is in the contrary direction to B layer. Whereas the 3R phase follows AA stacking order that makes it maintain the broken inversion symmetry as monolayers.^[39] It is worth mentioning that 3R bilayer WS_2 suppresses the interlayer hopping interaction due to the localized wave function (See schematic of 3R-stacking bilayer that only intralayer exciton formed),^[30,40] which leads to many novel properties such as maintaining a high valley polarization degree, etc., comparing with the 2H one.^[41] In our work, we first applied the second harmonic generation (SHG) spectroscopy to determine the stacking order of the two types bilayer WS_2 . As shown in **Figure 1b**, the SHG intensity of 3R bilayer WS_2 is twice that of monolayer, and the 2H-stacked bilayer shows no SHG signal due to the restored inversion symmetry. Besides, the sixfold SHG intensity pattern in polarization-dependent SHG spectrum suggests the threefold symmetry of monolayer and 3R-stacking bilayer WS_2 (see **Figure S2**, Supporting Information), which is consistent with the literature reported.^[40,42] The Raman and photoluminescence (PL) spectra of different WS_2 samples were further employed to analyze the difference of electronic band structures induced by stacking-order.^[25,43] In **Figure 1c**, a peak appears at 632 nm, which corresponds to A exciton of direct bandgap of monolayer WS_2 . The peak position exhibits a gradual redshift trend and the peak intensity also decreases significantly with the increase of the number of layers to bilayers. Interestingly, the indirect bandgap-induced emission peak (marked as I) exhibits different peak positions (729 and 738 nm) in 2H and 3R bilayer WS_2 , respectively, which can be attributed to the different interlayer electronic coupling between them.^[40] Since the energy of indirect bandgap transition reflects the electronic structure stability and the interlayer coupling strength, the redshift peak I in 3R bilayer WS_2 suggests a stronger interlayer coupling strength compared to 2H-stacking (see black dashed line in **Figure 1c,d**),^[25] exhibiting the low-frequency Raman spectra of WS_2 excited by 457 nm laser under the same excitation power at room temperature. The shear mode (S) at $\approx 18\text{ cm}^{-1}$ and layer-breathing mode (LB) at $\approx 32\text{ cm}^{-1}$ of the two bilayer WS_2 are clearly distinct from monolayer,^[44] and the two modes exhibit slightly redshift frequency for 3R-bilayer, which is probably related to the interlayer coupling strength as reported in previous literature.^[45,46] Intriguingly, an obvious increased intensity ratio between LB and S in 3R-bilayer WS_2 helps us to distinguish the two different layer-stacking configurations.^[43,46] In addition, we also obtained the high-frequency Raman spectra of different type of WS_2 under the same excitation condition. As presented in **Figure S3** (Supporting Information), we can clearly observe two characteristic Raman modes, the in-plane vibration E_{2g}^1 mode ($\approx 357\text{ cm}^{-1}$) and the out-of-plane vibration A_{1g} mode ($\approx 420\text{ cm}^{-1}$), which coincide with the reported results.^[40,47] All these results indicate that these

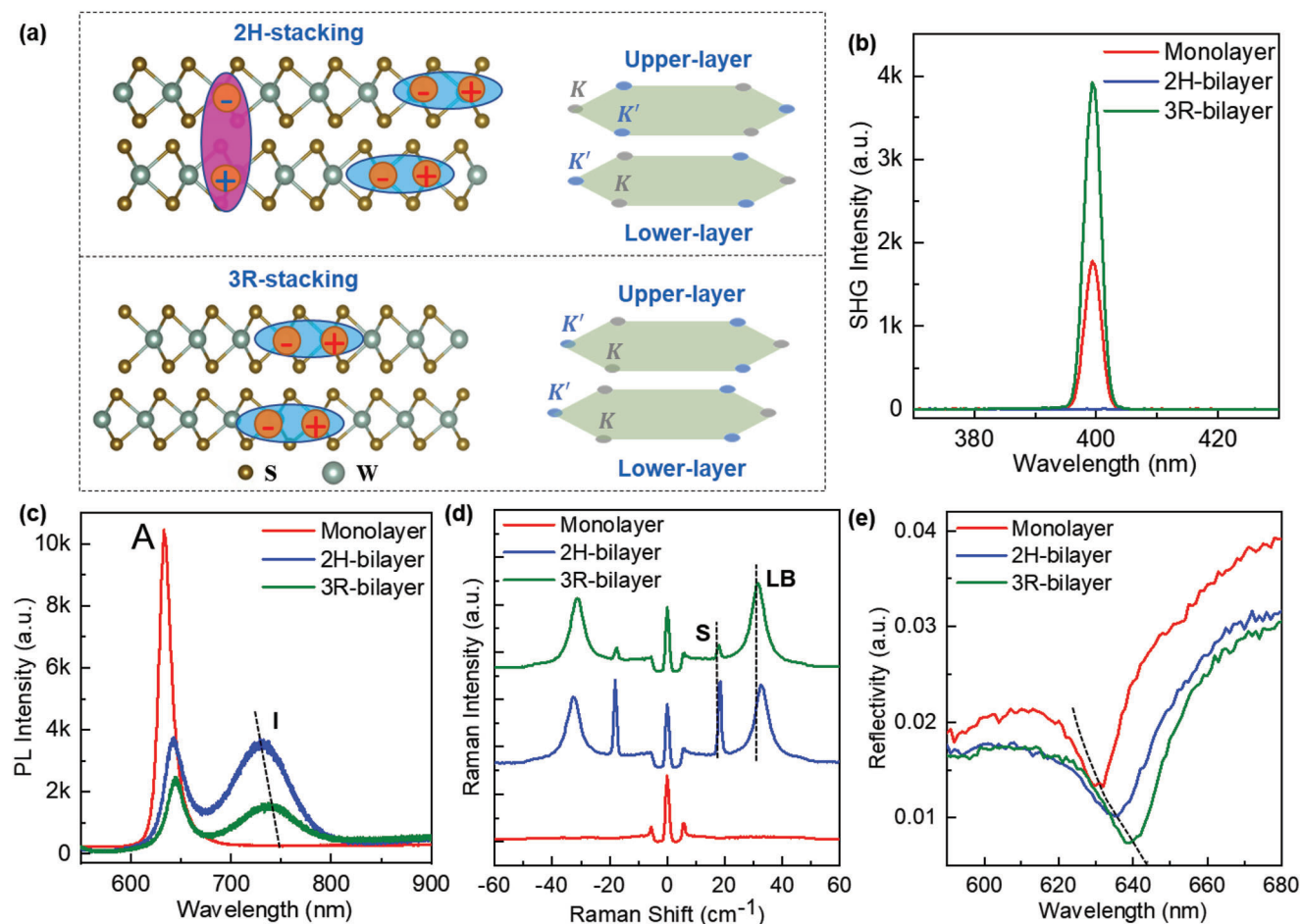


Figure 1. a) Side view of atomic structure and an illustration in momentum space for 2H and 3R-stacking bilayer WS₂. 2H-stacking includes the interlayer hopping interaction while the hopping is suppressed in 3R-stacking WS₂. For the 2H-stacking, K valley is on top of K' valley, while K valley is on top of K valley in 3R-stacking. b) The second harmonic generation (SHG) spectra of different layer WS₂. c) PL spectra of different layer WS₂. A and I represent the direct bandgap and indirect bandgap transition peak, respectively. d) Low-frequency Raman spectra of different layer WS₂. S and LB denote the shear and layer-breathing mode. e) Room-temperature reflection spectra of different layer WS₂. The black-dashed line indicates the redshift of A-exciton peak.

two bilayer WS₂ are of high quality and stable at room temperature, and they belong to the 2H and 3R phase, respectively, with different interlayer coupling strengths. Then, room-temperature reflection spectra of monolayer, 2H and 3R bilayer WS₂ were carried out to investigate the linewidth broadening effect. As can be seen from Figure 1e, monolayer, 2H and 3R bilayer WS₂ show a gradual redshift trend, which is related to the emergence of interlayer coupling and the change of interlayer coupling strength. However, the signal intensity in the reflection spectrum at room temperature is relatively weak, and the extraction of linewidth of the excitonic state limits the accuracy of the research due to the influence of substrate signals. Therefore, in the follow-up experiments, we conducted a comparative analysis of the temperature-dependent reflectance spectrum and MCD spectrum, trying to explore the different exciton-phonon coupling behaviors caused by the appearance of interlayer coupling as well as the different interlayer coupling strength in 2H and 3R bilayer WS₂ compared to monolayers.

On the basis of the previous analysis, the low temperature (77 K) reflection and MCD spectra of 2H and 3R-stacking bi-

layer WS₂ under different external magnetic fields have been carried out. Figure 2a,c exhibits the reflection and MCD spectra of monolayer, 2H-stacking and 3R-stacking bilayer WS₂ at 77 K under -4 T magnetic field. As can be seen from reflection spectra in Figure 2a, three apparent valleys are observed at 2.035, 2.02, and 2.006 eV, which correspond to the transition of A exciton in monolayer, 2H and 3R-stacking bilayer WS₂ separately. In addition, a small valley in the vicinity of 2.12 eV appears in reflection spectra, which originates from the light source system and can be eliminated in MCD system. Although the measurement was performed at lower temperature 77 K, the signal of reflection spectra was still weaker and the exciton peak was superimposed on the stronger background. The non-zero baseline mode will lead to the larger uncertainty on the linewidth extraction. As shown in Figure S4 (Supporting Information), by selecting two different types of baseline mode for Gaussian fitting of the reflection spectrum via origin software, we can obtain the approximate value of linewidth. And based on the smoothing baseline mode, the linewidth of monolayer, 2H and 3R-stacking bilayer WS₂ shown in Table S1 (Supporting Information) are 25.2, 36.6,

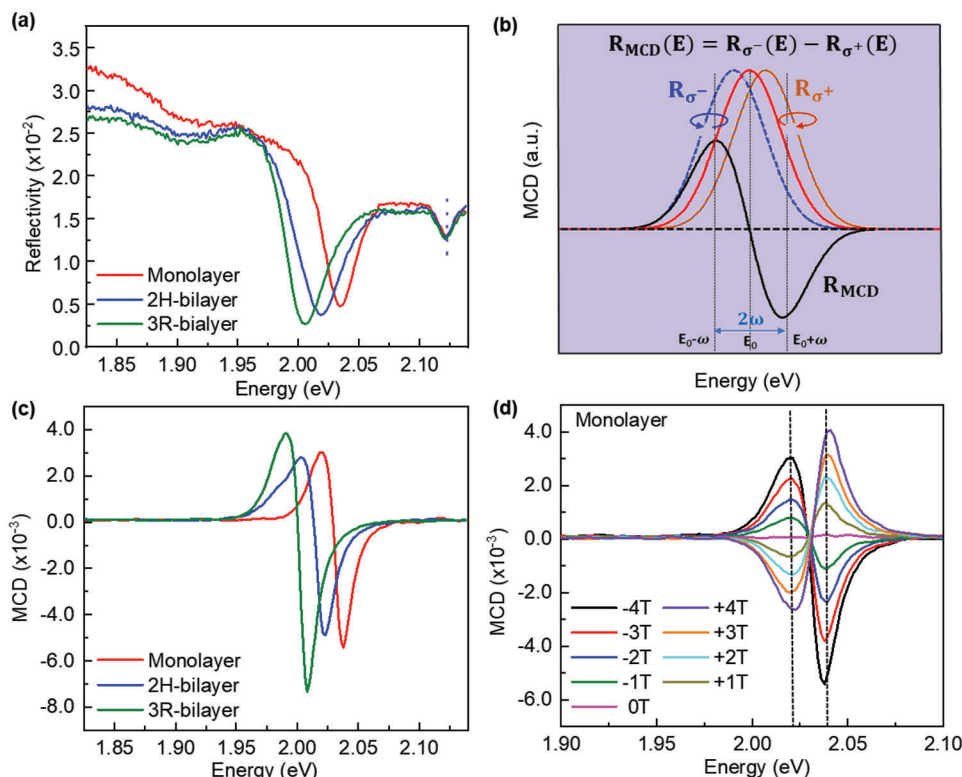


Figure 2. a) Reflection spectra of different layer WS_2 under a -4 T magnetic field at 77 K. b) Measurement principle of MCD system, which represents the reflection spectrum difference between LCP (R_{σ^-}) and RCP (R_{σ^+}) light. c) Corresponding MCD spectra of different layer WS_2 . d) MCD spectra of monolayer WS_2 recorded at 77 K and applied magnetic field ranges from -4 to 4 T.

and 32.5 meV, respectively, which exists a 2 meV or even larger uncertainty of fitting due to the strong background signal and poor signal-noise ratio (SNR) induced unclear baseline extraction. In contrast, according to the principle of MCD testing in Figure 2b, MCD signal can be regarded as the first-order differential of modulated reflection spectrum and presented as an antisymmetric shape.^[35] Here, the exciton peak position E_0 and linewidth 2ω can be obtained by measuring the distance between negative valley and positive peak of MCD spectrum, in which E_0 and 2ω are defined as $E_0 = \frac{E_1 + E_2}{2}$, $2\omega = |E_1 - E_2|$, respectively. (E_1 represents the valley position, E_2 represents the peak position. 2ω can be defined as full width at half maximum (FWHM), where FWHM usually denotes the spectra width obtained by Gaussian fitting). As displayed in Figure 2c, by eliminating the influence of background signals that are unrelated to excitons in experiments, we can obtain the transition energy and linewidth of A exciton in monolayer, 2H and 3R-stacking bilayer WS_2 directly and precisely according to the zero and extreme points of MCD signals. It is obvious that the A exciton peak exhibits a gradual redshift for the monolayer, 2H and 3R-stacking bilayer that can be clearly seen from zero points in MCD spectra. The redshift of peak positions from monolayer to bilayer is due to the change of band structure caused by the occurrence of interlayer coupling, while the redshift peak position of 3R bilayer compared with the 2H one is due to the different interlayer coupling strength caused by the different stacking orders, which is closely related to the distinction of their band structure.^[48,49] It should be noted that

theoretically there is a small splitting for the A exciton in 3R bilayer WS_2 , which is not distinguishable in the current experimental conditions.^[31] And it is valuable to be further studied in the future work. Significantly, we can easily obtain the accurate exciton linewidth of monolayer, 2H and 3R-stacking bilayer WS_2 ≈ 18.1 , 19.9, and 18.9 meV according to the position of extreme points in MCD spectra. As shown in Figure S5 (Supporting Information), comparing with the first differential reflectance spectra ($\Delta R/R$) that directly differentiate all the signals mathematically, the MCD measurement can remarkably improve the SNR and obtain narrower linewidth by excluding the independent factor of exciton linewidth. This is because the MCD signal originates from the Zeeman splitting of exciton under the applied magnetic field that is perpendicular to the sample surface, which breaks the valley degeneracy and reflects the modulation of the energy band structure by the magnetic field. The transition probability difference of the left and right circular polarized photons brings about the reflection spectrum difference between LCP and RCP and leads to the antisymmetric MCD signal that stems from the first-order differentiated exciton reflection signals. Importantly, as can be seen from Figure 2d and Figure S6 (Supporting Information), the SNR of reflection spectrum does not change due to the appearance and change of the magnetic field. While the linewidth of the A excitons is uniform in the MCD spectrum of WS_2 as the change of the magnetic field, SNR of the signal is significantly enhanced. This means that using MCD spectroscopy can effectively exclude the background signals that unrelated to the exciton

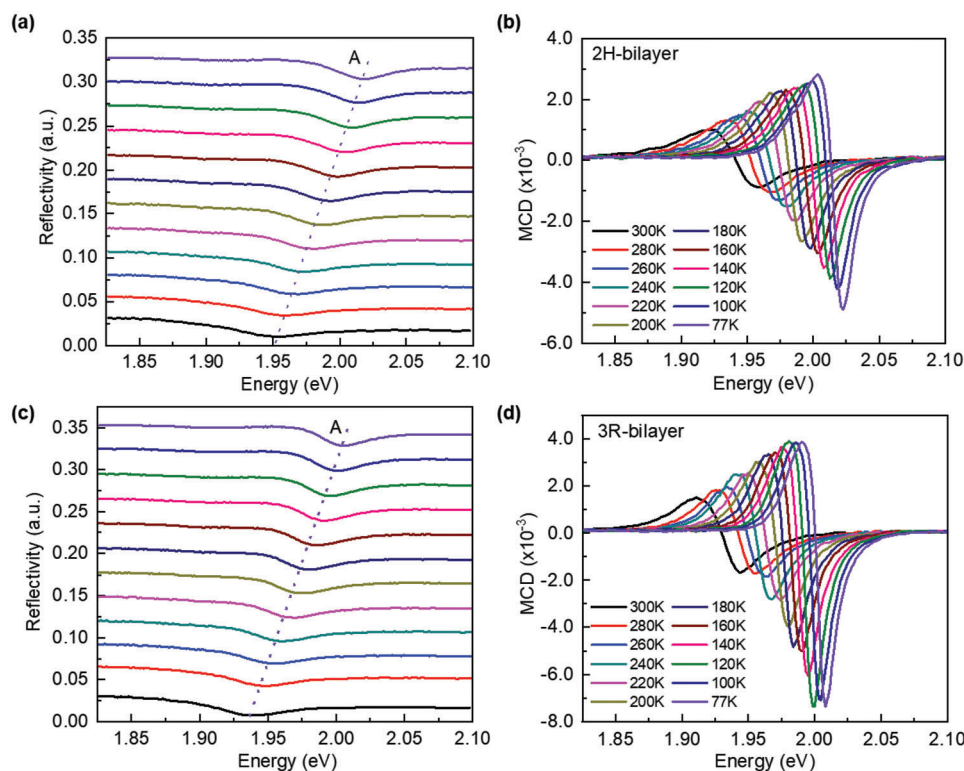


Figure 3. a,c) Temperature-dependent reflection spectra of 2H and 3R-stacking bilayer WS_2 under -4 T magnetic field. b,d) Corresponding MCD spectra of 2H and 3R-stacking WS_2 at the same temperature range.

linewidth, such as the roughness, cleanliness of the substrate surface, and the substrate induced disorder effect, which have nothing to do with exciton transitions and do not contribute to the MCD signal. Besides, the external magnetic field does not cause additional linewidth broadening, that is, the negative valley and positive peak of MCD signal are exhibited at the same position. These advantages of MCD spectrum can help us to conduct more in-depth studies of exciton linewidth in WS_2 .

To distinguish the contributions of linewidth broadening, including temperature-independent and thermally activated phonon-assisted processes, we performed temperature-dependent MCD measurements. **Figure 3a,c** depicts the reflection spectra of 2H and 3R-stacking bilayer WS_2 at variable temperatures from 77 to 300 K under -4 T magnetic field, from which the absorption peak of A exciton can be distinguished. We also observed the blueshift peak and narrower linewidth of A exciton by decreasing the temperature. Even with the improved SNR of the reflection spectra at low temperature, the signal of the reflection peak is still superimposed on the strong background, which is likely to originate from the physical processes that are independent of exciton transitions such as the defects, unintentional impurities, or the substrate effects. Thus, it is difficult to obtain the precise exciton peak position and linewidth from the reflection spectra, which is adverse to investigate the exciton peak position and linewidth difference induced by different interlayer coupling in 2H and 3R-stacking bilayer WS_2 .

Therefore, we performed the temperature-dependent MCD spectra of 2H and 3R-stacking bilayer WS_2 under the same experimental conditions, as presented in **Figure 3b,d**. The zero point

of the MCD signal corresponds to the peak position of A exciton in the reflection spectra, and a blueshift of the peak position can be clearly observed with decreasing temperature. The trend is consistent with that of temperature-dependent reflection spectra. Importantly, the linewidth becomes narrower and the characteristic signal intensity of MCD becomes larger as the temperature decreases. The signal line-shape of MCD spectra appears as peak-valley feature with some asymmetry, which we believe is due to the fact that the density of states allowed by the transition is not ideally symmetric at the K point. Finally, we obtained the accurate exciton energy and linewidth of A exciton in 2H and 3R-stacking bilayer WS_2 extracted from the temperature-dependent MCD spectra. In order to analyze the exciton-phonon coupling difference between bilayer and monolayer, we also measured the reflection and MCD spectra of the monolayer WS_2 . As displayed in **Figure S7** (Supporting Information), the exciton peak position and linewidth follow the same relative trend at different temperatures, and the specific differences will be discussed in the following.

As shown in **Figure 4a**, we can quantitatively obtain the transition energy of A excitons from the MCD spectra of different layered WS_2 with the temperature ranging from 77 to 300 K. We find that the A exciton peak behaves redshift with increasing temperature, which can be attributed to the shrinking electronic bandgap caused by lattice expansion and the energy renormalization caused by exciton-phonon interactions. The temperature-dependent exciton peaks in different-layer WS_2 can be well fitted by Varshni equation effectively,^[50] which provides an empirical description of the energy change in the semiconductor bandgap.

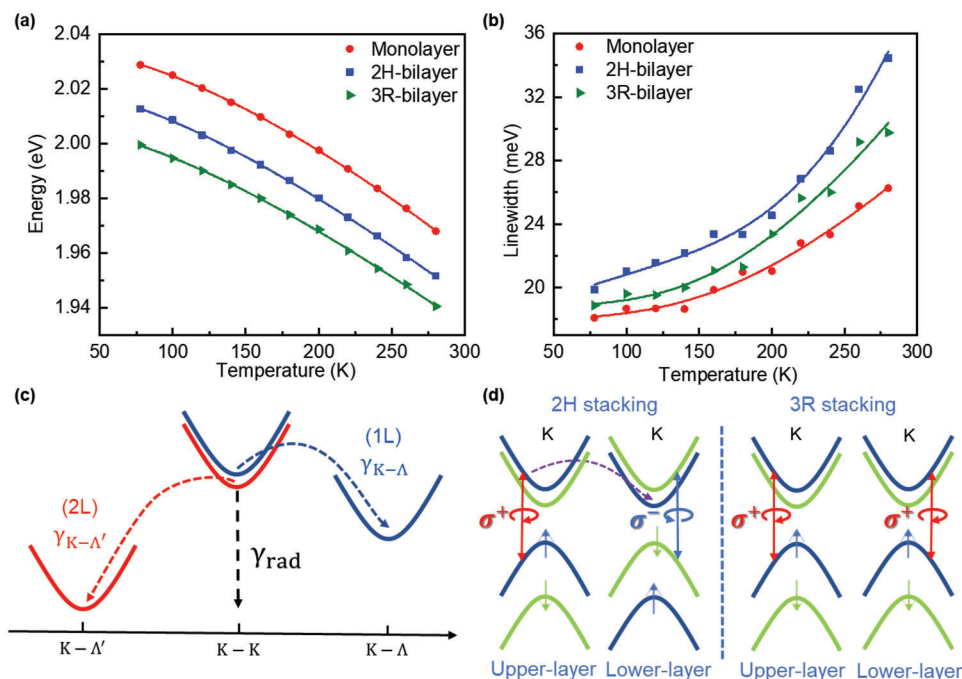


Figure 4. a) Plot of peak energy of A exciton versus temperature in different layer WS₂ extracted from MCD spectra and the data was fitted by utilizing Varshni equation. b) The A exciton linewidths of different layer WS₂ extracted from MCD spectra are plotted as a function of temperature. c) A brief schematic diagram of parabolic minima of exciton dispersion in monolayer and bilayer WS₂ as a function of center-of-mass momentum. d) Schematic illustration of band structures and K-valley transition selection rules that A-exciton complied in 2H and 3R-stacking bilayer. σ^+ (σ^-) denotes the right (left) circularly polarized light, and the purple arrow in 2H-stacking bilayer indicates the interlayer hopping between upper and lower layers.

Table 1. Varshni fitting parameters that describe the temperature dependence of A exciton transition energies for monolayer, 2H and 3R-stacking bilayer WS₂.

Varshni fitting parameters	A exciton [Monolayer]	A exciton [2H-bilayer]	A exciton [3R-bilayer]
$E(0)/\text{eV}$	2.036	2.02	2.01
$\alpha/\text{meV K}^{-1}$	0.66	0.5	0.49
β/K	478.9	283.8	299.5

The Varshni equation can be expressed as

$$E(T) = E(0) - \frac{\alpha T^2}{T + \beta} \quad (1)$$

where $E(0)$ is the exciton transition energy at the limit of zero temperature, α and β are the Varshni parameter, α is relevant to the crystal lattice and indicates the strength of exciton-phonon coupling, while β is closely related to the Debye temperature. The fitted parameter values of the temperature-dependent exciton energy using the Varshni equation are presented in the **Table 1**. The $E(0)$ we obtained displays a gradually redshifted trend from monolayer, 2H-bilayer to 3R-bilayer, which stems from the difference of band structure between bilayer and monolayer, and the distinction of interlayer coupling between 2H and 3R bilayer. Besides, it is interesting that the two temperature-related parameters α and β are highly similar for both 2H and 3R-stacking bilayer, while the difference for bilayer comparing

with monolayer may be originated from the small interlayer interaction.^[31] From Figure 4b, we can observe that the exciton linewidths display a non-linear increase at the whole temperature for the monolayer, 2H and 3R-stacking bilayer WS₂ samples, respectively. It is worth noting that the linewidth in 3R-bilayer always exhibits narrower linewidth than 2H-bilayer at the same temperature, which could be related to the different interlayer coupling induced by stacking sequence. We can acquire the linewidth of 32.3, 39.8, and 35.3 meV in monolayer, 2H and 3R-stacking bilayer at room temperature, which all exhibit extra linewidth broadening in comparison to those at 77 K due to the temperature-induced phonon scattering.

In order to estimate the influence of exciton-phonon coupling in linewidth broadening, we describe the temperature-dependent linewidth broadening by the listed expression that is derived from the excitonic effects in GaAs quantum wells.^[51–53]

$$\Gamma(T) = \Gamma(0) + \gamma_1 T + \frac{\gamma_2}{\exp\left(\frac{\Omega}{k_B T}\right) - 1} \quad (2)$$

Where the first term $\Gamma(0)$ indicates the broadening originated from temperature-independent mechanisms; the second linearity term is attributed to the exciton-acoustic phonon interaction and the coefficient γ_1 represents the acoustic-phonon coupling constant; whereas the third term corresponds to the interaction of excitons with optical phonons at the corners of the Brillouin zone or acoustic phonons at the Brillouin zone edges, γ_2 represents the strength of exciton-phonon coupling, and Ω represents

Table 2. Linewidth fitting parameters that describe the temperature dependence of A exciton linewidth broadening for mono-layer, 2H and 3R-stacking bilayer WS₂.

Linewidth fitting parameters	A exciton [Monolayer]	A exciton [2H-bilayer]	A exciton [3R-bilayer]
$\Gamma(0)/\text{meV}$	17.5	18	18.5
$\gamma_1/\mu\text{eVK}^{-1}$	8.02	28.4	7.08
γ_2/meV	73 ± 12	916 ± 100	111 ± 20
Ω/meV	60	112	60

the average energy of relevant effective phonons. The linewidth fitting parameters that describe the temperature dependence of A exciton linewidth broadening for different layer WS₂ are displayed in Table 2.

For the monolayer, 2H and 3R-stacking bilayer WS₂, we derive a temperature-independent term $\Gamma(0)$, respectively, the linewidth predominantly stems from the radiative decay contribution and the numerical value is of the same magnitude order that obtained in the reference for monolayer TMDs based on the photoluminescence, reflection spectra, and Raman scattering measurement, etc.^[19,20,54–62] In addition, the obtained value of effective phonons energy Ω between monolayer and 3R bilayer are highly consistent, but it is twice in 2H bilayer as much as in monolayer and 3R bilayer. The results suggest that there probably exists more phonon-assistant scattering channels in 2H-bilayer comparing with monolayer and 3R bilayer. It is worth noting that the linearity coefficient γ_1 we obtained for monolayer and 3R-stacking bilayer are almost the same, while it is much larger for the 2H-stacking bilayer. It is shown that the efficient exciton-acoustic phonon scattering within K valley is much stronger in 2H stacking bilayer due to the intravalley transfer of carriers between layers. Significantly, the super-linear increase of linewidth in 2H stacking bilayer is much faster than monolayer and 3R-stacking bilayer that can be seen from Figure 4b. This is due to the remarkably different behaviors for the contribution of K – Λ , K – Λ' intervalley scattering in bilayer as compared to monolayer.^[60] As shown in Figure 4c, the main exciton scattering channels including radiative and intervalley scattering contributions are indicated by dashed arrows. Here, we only consider the exciton states with the same spin, the red- and blue-dashed arrows denote the possible inelastic intervalley scattering processes in different layer WS₂, and the black-dashed arrows indicate the radiative contribution. Our results show that the exciton-optical phonon coupling constant $\gamma_2 = (73 \pm 12)$ meV, (916 ± 100) meV for monolayer and 2H-stacking bilayer, which is an order of magnitude larger in bilayer compared with monolayer and the results stem from the prominent change of phonon-assisted intervalley scattering channels in bilayer. As the reference reported, the Λ and Λ' valley-splitting of the lowest conduction band state with opposite spin in bilayer is determined by interlayer coupling while the spin-orbit coupling plays the decisive role in monolayer,^[63] which makes the K – Λ' intervalley scattering the dominant channel in bilayer, while K – Λ intervalley scattering channel is largely responsible for monolayer. What is more, the exciton-optical phonon coupling constant $\gamma_2 = (916 \pm 100)$ meV of 2H-stacking bilayer WS₂ is also much larger in comparison to that $\gamma_2 = (111 \pm 20)$ meV of 3R-stacking bilayer. As illustrated schemat-

ically in Figure 4d, for the 2H-stacking bilayer, the σ^+ circularly polarized light can only excite the K-valley transition of the upper layer, but the interlayer hopping process involves an additional intravalley transition from one layer to the other layer via phonon scattering.^[31,41] While for the 3R-stacking bilayer, the excitation of a given σ^+ circularly polarized light will result in the K-valley excitation of both upper and lower layers, which preserve the same spin-valley locking properties as for the monolayer case. Therefore, we believe that the additional interlayer scattering channel within K-valley in 2H-stacking bilayer can lead to the linewidth-broadening.

3. Conclusion

In summary, we have investigated the temperature-dependent linewidth broadening of CVD-grown 2H and 3R-stacking bilayer WS₂ compared with monolayer based on MCD spectrum. We got the quantitative results of exciton-phonon coupling strength and showed that the linewidth broadening of bilayer is markedly larger than monolayer, which originates from the significant change of phonon-assisted relaxation channels in bilayer. Significantly, we found that 3R-stacking bilayer WS₂ with a larger A-exciton peak redshift displays narrower linewidth in comparison to 2H-stacking, which can be ascribed to the additional interlayer scattering channel within K-valley in 2H-stacking bilayer. Our work demonstrated a powerful new method to study the difference of stacking-order induced interlayer coupling as well as the exciton scattering mechanism, and the results inspire us to explore the possibility of future narrow-linewidth 2D sensors and emitters devices.

4. Experimental Section

Sample Preparation: WS₂ was prepared at the temperature of ≈ 750 – 850 °C. The alumina crucible containing 6 mg NaCl and 30 mg WO₃ was placed in the center of the tube. The furnace was heated with a ramp rate of 50 °C min^{-1} to the growth temperature (750 – 850 °C) and held for 3 min. The Ar/H₂ (80/10 sccm) was used as the carrier gas.

Optical Measurements: Raman spectra were collected by a Horiba HR800 system with an excitation wavelength of 457 nm. The SHG measurements were conducted on a femtosecond laser integrated microscope (Nikon, Eclipse Ti) with $100\times$ (NA = 0.9) objective lens. The excitation source for measuring SHG is a femtosecond laser pulse with wavelength of 800 nm and repetition rate of 80 MHz generated by Ti:sapphire oscillator. The MCD measurement was performed using a wavelength tunable laser via a supercontinuum white light source equipped with a monochromator (Horiba Jobin-Yvon iHR320). The reflected light from the sample was detected using a Si photodetector. The reflectance and MCD signals were obtained using two lock-in amplifiers with reference frequencies of a 177 Hz chopper and a 50 kHz photoelastic modulator, respectively. The schematic diagram of MCD configuration is shown in Figure S1b (Supporting Information). Besides, out-of-plane applied magnetic fields along the incident direction of the excitation laser were provided by a superconducting magnet. (manufactured by CyroMagnetics company).

Supporting Information

Supporting Information is available from the Wiley Online Library or from the author.

Acknowledgements

N.J. and J.S. contributed equally to this work. The authors gratefully acknowledge the support from the Youth Innovation Promotion Association, Chinese Academy of Sciences (2019114), and the Strategic Priority Research Program of the Chinese Academy of Sciences (XDB30000000).

Conflict of Interest

The authors declare no conflict of interest.

Data Availability Statement

The data that support the findings of this study are available from the corresponding author upon reasonable request.

Keywords

CVD-grown, exciton-phonon interaction, interlayer hopping, magnetic circular dichroism, stacking-order

Received: February 23, 2023
Revised: April 20, 2023
Published online: May 17, 2023

- [1] Q. H. Wang, K. Kalantar-Zadeh, A. Kis, J. N. Coleman, M. S. Strano, *Nat. Nanotechnol.* **2012**, *7*, 699.
- [2] J. Xiao, M. Zhao, Y. Wang, X. Zhang, *Nanophotonics*. **2017**, *6*, 1309.
- [3] W. Xu, W. Liu, J. F. Schmidt, W. Zhao, X. Lu, T. Raab, C. Diederichs, W. Gao, D. V. Seletskiy, Q. Xiong, *Nature* **2017**, *541*, 62.
- [4] K. F. Mak, C. Lee, J. Hone, J. Shan, T. F. Heinz, *Phys. Rev. Lett.* **2010**, *105*, 136805.
- [5] I. G. Lezama, A. Arora, A. Ubaldini, C. Barreateau, E. Giannini, M. Potemski, A. F. Morpurgo, *Nano Lett.* **2015**, *15*, 2336.
- [6] H. P. Komsa, A. V. Krasheninnikov, *Phys. Rev. B* **2012**, *86*, 241201(R).
- [7] A. T. Hanbicki, M. Currie, G. Kioseoglou, A. L. Friedman, B. T. Jonker, *Solid State Commun.* **2015**, *203*, 16.
- [8] A. F. Rigosi, H. M. Hill, K. T. Rim, G. W. Flynn, T. F. Heinz, *Phys. Rev. B* **2016**, *94*, 075440.
- [9] K. He, N. Kumar, L. Zhao, Z. Wang, K. F. Mak, H. Zhao, J. Shan, *Phys. Rev. Lett.* **2014**, *113*, 026803.
- [10] A. Chernikov, T. C. Berkelbach, H. M. Hill, A. Rigosi, Y. Li, O. B. Aslan, D. R. Reichman, M. S. Hybertsen, T. F. Heinz, *Phys. Rev. Lett.* **2014**, *113*, 076802.
- [11] A. Ramasubramaniam, *Phys. Rev. B* **2012**, *86*, 115409.
- [12] T. Jakubczyk, K. Nogajewski, M. R. Molas, M. Bartos, W. Langbein, M. Potemski, J. Kasprzak, *2D Mater.* **2018**, *5*, 031007.
- [13] I. Paradisanos, G. Wang, E. M. Alexeev, A. R. Cadore, X. Marie, A. C. Ferrari, M. M. Glazov, B. Urbaszek, *Nat. Commun.* **2021**, *12*, 538.
- [14] Z. Wang, A. Molina-Sánchez, P. Altmann, D. Sangalli, D. De Fazio, G. Soavi, U. Sassi, F. Bottegoni, F. Ciccacci, M. Finazzi, L. Wirtz, A. C. Ferrari, A. Marini, G. Cerullo, S. Dal Conte, *Nano Lett.* **2018**, *18*, 6882.
- [15] L. Yuan, L. B. Huang, *Nanoscale* **2015**, *7*, 7402.
- [16] W. J. Zhao, R. M. Ribeiro, M. Toh, A. Carvalho, C. Kloc, A. H. Castro Neto, G. Eda, *Nano Lett.* **2013**, *13*, 5627.
- [17] K. Kaasbjerg, K. S. Thygesen, K. W. Jacobsen, *Phys. Rev. B* **2012**, *85*, 115317.
- [18] Z. Jin, X. Li, J. T. Mullen, K. W. Kim, *Phys. Rev. B* **2014**, *90*, 045422.
- [19] M. Selig, G. Berghäuser, A. Raja, P. Nagler, C. Schuller, T. F. Heinz, T. Korn, A. Chernikov, E. Malic, A. Knorr, *Nat. Commun.* **2016**, *7*, 13279.
- [20] B. R. Carvalho, Y. Wang, S. Mignuzzi, D. Roy, M. Terrones, C. Fantini, V. H. Crespi, L. M. Malard, M. A. Pimenta, *Nat. Commun.* **2017**, *8*, 14670.
- [21] X. X. Zhang, Y. M. You, S. Y. F. Zhao, T. F. Heinz, *Phys. Rev. Lett.* **2015**, *115*, 257403.
- [22] A. Arora, M. Koperski, K. Nogajewski, J. Marcus, C. Faugeras, M. Potemski, *Nanoscale* **2015**, *7*, 104219.
- [23] M. Kira, S. W. Koch, *Prog. Quantum Electron.* **2006**, *30*, 155.
- [24] M. Xia, B. Li, K. Yin, G. Capellini, G. Niu, Y. Gong, W. Zhou, P. M. Ajayan, Y. H. Xie, *ACS Nano* **2015**, *9*, 12246.
- [25] K. Liu, L. Zhang, T. Cao, C. Jin, D. Qiu, Q. Zhou, A. Zettl, P. Yang, S. G. Louie, F. Wang, *Nat. Commun.* **2014**, *5*, 4966.
- [26] W. T. Hsu, Z. A. Zhao, L. J. Li, C. H. Chen, M. H. Chiu, P. S. Chang, Y. C. Chou, W. H. Chang, *ACS Nano* **2014**, *8*, 2951.
- [27] P. C. Yeh, W. Jin, N. Zaki, J. Kunstmann, D. Chenet, G. Arefe, J. T. Sadowski, J. I. Dadap, P. Sutter, J. Hone, *Nano Lett.* **2016**, *16*, 953.
- [28] S. Huang, L. Liang, X. Ling, A. A. Puzos, D. B. Geohegan, B. G. Sumpter, J. Kong, V. Meunier, M. S. Dresselhaus, *Nano Lett.* **2016**, *16*, 1435.
- [29] S. Shinde, K. Dhakal, X. Chen, W. Yun, J. Lee, H. Kim, J. Ahn, *NPG Asia Mater.* **2018**, *10*, e468.
- [30] I. Paradisanos, S. Shree, A. George, N. Leisgang, C. Robert, K. Watanabe, T. Taniguchi, R. Warburton, A. Turchanin, X. Marie, I. Gerber, B. Urbaszek, *Nat. Commun.* **2020**, *11*, 2391.
- [31] L. M. Schneider, J. Kuhnert, S. Schmitt, W. Heimbrod, U. Huttner, L. Meckbach, T. Stroucken, S. W. Koch, S. Fu, X. Wang, K. Kang, E. Yang, A. Rahimi-Iman, *J. Phys. Chem. C* **2019**, *123*, 21813.
- [32] F. H. Shao, S. Y. Woo, N. Wu, R. Schneider, A. J. Mayne, S. M. de Vasconcellos, A. Arora, B. J. Carey, J. A. Preuß, N. Bonnet, M. Och, C. Mattevi, K. Watanabe, T. Taniguchi, Z. C. Niu, R. Bratschitsch, Tizei, L. H. G., *Phys. Rev. Mater.* **2022**, *6*, 074005.
- [33] Z. Khatibi, M. Feierabend, M. Selig, S. Brem, C. Linderalv, P. Erhart, E. Malic, *2D Mater.* **2019**, *6*, 015015.
- [34] J. Fang, K. Yao, T. Y. Zhang, M. S. Wang, T. Z. Jiang, S. C. Huang, B. A. Korgel, M. Terrones, A. Alù, Y. B. Zheng, *Adv. Mater.* **2022**, *34*, 2108721.
- [35] Y. J. Wu, C. Shen, Q. H. Tan, J. Shi, X. F. Liu, Z. H. Wu, J. Zhang, P. H. Tan, H. Z. Zheng, *Appl. Phys. Lett.* **2018**, *112*, 153105.
- [36] Y. Lee, X. Zhang, W. Zhang, M. Chang, C. Lin, K. Chang, Y. Yu, J. Wang, C. Chang, L. Li, T. Lin, *Adv. Mater.* **2012**, *24*, 2320.
- [37] A. Antonelou, T. Hoffman, J. H. Edgar, S. N. Yannopoulos, *J. Mater. Sci.* **2017**, *52*, 7028.
- [38] S. Shree, A. George, T. Lehnert, C. Neumann, M. Benelajla, C. Robert, X. Marie, K. Watanabe, T. Taniguchi, U. Kaiser, B. Urbaszek, A. Turchanin, *2D Mater.* **2019**, *7*, 015011.
- [39] J. Shi, P. Yu, F. Liu, P. He, R. Wang, L. Qin, J. Zhou, X. Li, J. Zhou, X. Sui, S. Zhang, Y. Zhang, Q. Zhang, T. Sum, X. Qiu, Z. Liu, X. Liu, *Adv. Mater.* **2017**, *29*, 1701486.
- [40] Z. Zeng, X. Sun, D. Zhang, W. Zheng, X. Fan, M. He, T. Xu, L. Sun, X. Wang, A. Pan, *Adv. Funct. Mater.* **2019**, *29*, 1806874.
- [41] L. Du, J. Tang, J. Liang, M. Liao, Z. Jia, Q. Zhang, Y. Zhao, R. Yang, D. Shi, L. Gu, J. Xiang, K. Liu, Z. Sun, G. Zhang, *Research* **2019**, *2019*, 6494565.
- [42] M. Zhao, Z. Ye, R. Suzuki, Y. Ye, H. Zhu, J. Xiao, Y. Wang, Y. Lwasa, X. Zhang, *Light: Sci. & Appl.* **2016**, *5*, e16131.
- [43] M. L. L., Q. H. T., J. B. Wu, X. S. C., J. H. W., Y. H. Pan, X. Zhang, X. Cong, J. Zhang, W. Ji, P. A. H. u., K. H. L., P. H. Tan, *ACS Nano* **2018**, *12*, 8770.
- [44] Y. Jinho, L. Jae-Ung, C. Hyeonsik, *Flat Chem* **2017**, *3*, 64.
- [45] J. He, K. Hummer, C. Franchini, *Phys. Rev. B* **2014**, *89*, 075409.
- [46] A. Puzos, L. Liang, X. Li, K. Xiao, K. Wang, M. Samani, L. Basile, J. Ldrobo, B. Sumpter, V. Meunier, D. Geohegan, *ACS Nano* **2015**, *9*, 6333.

- [47] R. Yang, S. Feng, X. Lei, X. Mao, A. Nie, B. Wang, K. Luo, J. Xiang, F. Wen, C. Mu, Z. Zhao, B. Xu, H. Zeng, Y. Tian, Z. Liu, *Nanotech.* **2019**, *30*, 345203.
- [48] S. Brem, K. Q. Lin, R. Gillen, J. M. Bauer, J. Maultzsch, J. M. Lupton, E. Malic, *Nanoscale* **2020**, *12*, 11088.
- [49] Z. J. Li, J. Förste, K. J. Watanabe, T. Taniguchi, B. Urbaszek, A. S. Baimuratov, I. C. Gerber, A. Högele, I. Bilgin, *Phys. Rev. B* **2022**, *106*, 045411.
- [50] N. M. Ravindra, V. K. Srivastava, *J. Phys. Chem. Solids* **1979**, *40*, 791.
- [51] S. Rudin, T. L. Reinecke, B. Segall, *Phys. Rev. B* **1990**, *42*, 11218.
- [52] A. V. Gopal, R. Kumar, A. S. Vengurlekar, T. Mélin, F. Laruelle, B. Etienne, *Appl. Phys. Lett.* **1999**, *74*, 2474.
- [53] A. V. Gopal, R. Kumar, A. S. Vengurlekar, A. Bosacchi, S. Franchi, L. N. Pfeiffer, *J. Appl. Phys.* **2000**, *87*, 1858.
- [54] S. Koirala, S. Mouri, Y. H. Miyauchi, K. Matsuda, *Phys. Rev. B* **2016**, *93*, 075411.
- [55] S. Helmrich, R. Schneider, A. W. Achtstein, A. Arora, B. Herzog, S. M. de Vasconcellos, M. Kolarczik, O. Schöps, R. Bratschitsch, U. Woggon, N. Owschimikow, *2D Mater.* **2018**, *5*, 045007.
- [56] D. Li, C. Trovatiello, S. Dal Conte, M. Nuss, G. Soavi, G. Wang, A. C. Ferrari, G. Cerullo, T. Brixner, *Nat. Commun.* **2021**, *12*, 954.
- [57] D. Erkensten, S. Brem, E. Malic, *Phys. Rev. B* **2021**, *103*, 045426.
- [58] B. R. Carvalho, L. M. Malard, J. M. Alves, C. Fantini, M. A. Pimenta, *Phys. Rev. Lett.* **2015**, *114*, 136403.
- [59] P. Soubelet, A. E. Bruchhausen, A. Fainstein, K. Nogajewski, C. Faugeras, *Phys. Rev. B* **2016**, *93*, 155407.
- [60] A. Raja, M. Selig, G. Berghäuser, J. Yu, H. M. Hill, A. F. Rigosi, L. E. Brus, A. Knorr, T. F. Heinz, E. Malic, A. Chernikov, *Nano Lett.* **2018**, *18*, 6135.
- [61] A. Arora, K. Nogajewski, M. Molas, M. Koperski, M. Potemski, *Nanoscale* **2015**, *7*, 20769.
- [62] S. Shree, M. Semina, C. Robert, B. Han, T. Amand, A. Balocchi, M. Manca, E. Courtade, X. Marie, T. Taniguchi, K. Watanabe, M. M. Glazov, B. Urbaszek, *Phys. Rev. B* **2018**, *98*, 035302.
- [63] R. Roldán, J. A. Silva-Guillén, M. P. López-Sancho, F. Guinea, E. Cappelluti, P. Ordejón, *Ann. Phys.-Berlin* **2014**, *526*, 347.